Chinese Physics Letters

LETTER

A Collision-State Criterion for Two-Peak Collisions in a Two-Dimensional Long-Wave–Short-Wave Resonance Interaction System

Cite as: Wei Dong *et al*. 2026 *Chin. Phys. Lett.* **43** 100403

DOI CSTR

Recommended Articles

Soliton Interactions and Collision Dynamics in a Variable-Coefficient Coupled Nonlocal Nonlinear Schrödinger Systems
Xinnan Cui, Zhiyang Zhang, Muwei Liu, Fenghua Qi, and Wenjun Liu
Chin. Phys. Lett. **42**, 100402 (2025)

An Off-Resonant Quantum Collision Model: Realizing a Qubit Coupled with an Effective Negative-Temperature Bath
Wei-Bin Yan, Zhong-Xiao Man, Ying-Jie Zhang, and Yun-Jie Xia
Chin. Phys. Lett. **42**, 010203 (2025)

Head-on Collision of Solitary Waves Described by the Toda Lattice Model in Granular Chain
Qianqian Wu, Xingyi Liu, Tengfei Jiao, Surajit Sen, and Decai Huang
Chin. Phys. Lett. **37**, 074501 (2020)

Relativistic Spherical Plasma Waves in a Collisional and Warm Plasma
Zhong-Kui Kuang, Li-Hong Cheng, Pan-Fei Geng, Rong-An Tang, and Ju-Kui Xue
Chin. Phys. Lett. **35**, 125202 (2018)

Stabilizing Rogue Waves in a Driven-Dissipative Nonlinear System
Chao Hang, and Guoxiang Huang
Chin. Phys. Lett. **43**, 020402 (2026)

Virtual Dirac Monopoles underlying the Nontrivial Phases of Rogue Waves
L.-C. Zhao, L.-Z. Meng, Y.-H. Qin, Z.-Y. Yang, and J. Liu
Chin. Phys. Lett. **42**, 110002 (2025)

A series journal of Chinese Physical Society distributed by IOP Publishing

Chinese Physics Letters

Chin. Phys. Lett. **43** 100403 (2026)

LETTER

DOI: 10.1088/0256-307X/43/10/100403
CSTR: 32039.14.0256-307X.43.10.100403

A Collision-State Criterion for Two-Peak Collisions in a Two-Dimensional Long-Wave–Short-Wave Resonance Interaction System

Wei Dong(董伟)[1], Houhui Yi(伊厚会)[2,*], Xiaofeng Li(李晓凤)[2], Muwei Liu(刘慕威)[3], and Zhiyang Zhang(张之阳)[3,*]

[1]Shandong Key Laboratory of Intelligent Manufacturing Technology for Advanced Power Equipment, School of Machinery and Automation, Weifang University, Weifang 261061, China
[2]School of Mechanical and Electrical Engineering, Weifang University of Science and Technology, Weifang 262700, China
[3]College of Physical Science and Technology, Beijing University of Posts and Telecommunications, Beijing 100876, China

[*]Corresponding authors. Email: houhuily@163.com; zzyang@bupt.edu.cn

This Letter investigates the finite-time morphology of two-pulse collisions in a two-dimensional long-wave–short-wave resonance interaction system with a local cubic perturbation. An integral identity for the centered second moment separates the collision dynamics into contributions from dispersive spreading, local quartic overlap, and long-wave feedback. For the prescribed two-sech initial-data family and the finite observation interval $T \leq 7$, these contributions distinguish double-peak and single-peak morphologies with an accuracy of 94.17%. A feedforward neural network is then employed to efficiently reconstruct the distribution of the identity-based result in the parameter plane of the nonintegrable coefficient and relative phase. This distribution shows that variation of the relative phase can change the collision morphology.

When two localized nonlinear waves remain well separated and interact only weakly, a multi-peak configuration may persist under small perturbations as a consequence of structural stability [1,2]. Such persistence, however, does not determine the outcome of a strong collision. Here we focus on counter-propagating pulses that undergo substantial spatial overlap, for which the post-collision field may either re-separate into a double-peak (DP) morphology or evolve into a single dominant peak. Recent studies report related localized pulse structures in nonlinear optical systems and further localized-wave and collision dynamics in coupled or resonant nonlinear-wave equations [3−5]. The resulting finite-time morphology is directly accessible in numerical simulations and experiments, making the selection between post-collision separation and merging a relevant question in nonlinear-wave dynamics.

The long-wave–short-wave resonance interaction (LSRI) system provides a clear model for this question. The resonance occurs when the phase velocity of a long wave equals the group velocity of a short-wave envelope [6,7]. Its standard one-dimensional integrable description is the Yajima–Oikawa (YO) system for sonic-Langmuir-wave resonance [8]. A related reduction applies to capillary–gravity wave packets [9]. The standard integrable two-dimensional LSRI system is a higher-dimensional extension [10], whose form is as follows:

$$\begin{aligned} &\mathrm{i}u_T - u_{XX} + Lu = 0, \\ &L_T = L_Y + 2(|u|^2)_X, \end{aligned} \tag{1}$$

where X and Y are spatial coordinates, T is the time variable, u is the complex short-wave envelope, and L is the real long-wave field. The integrable two-dimensional and multicomponent LSRI systems also support line-soliton and lump structures, including resonant lump-collision dynamics [11,12]. Short-wave dispersion acts along X, the long wave is transported along Y, and the two fields remain resonantly coupled. Bright-soliton collisions in integrable LSRI and YO systems have been classified [13−15]. Recent work has extended this picture to coupled LSRI models, semi-rational waves, breathers, and vector-soliton collisions [16−21]. Related two-dimensional and multicomponent equations also admit localized solitons, vortex structures, lumps, and multi-soliton interactions [22−29]. For exact solutions, however, the outgoing form is fixed by scattering data. This asymptotic description does not directly determine the finite-time morphology produced by a prescribed non-exact two-pulse initial state after strong collisional overlap.

Beyond the integrable setting, nonintegrable perturbations can produce localized finite-time structures [30]. Recent analytical and numerical studies also show varied soliton, breather, and collision dynamics in nonintegrable or higher-order nonlinear wave models [31−35]. Long-time behavior can instead be organized by Riemann–Hilbert analysis [36−38]. Those studies concern asymptotic limits of other integrable equations. For the specific scenario of strong collisions between the prescribed two-sech pulse superpositions considered here in the perturbed two-dimensional LSRI system, where collision outcomes bifurcate between post-collision separation and merging, an analytical criterion for predicting which morphology will be realized is still lacking.

This Letter addresses that question through a moment-based criterion. A local cubic envelope nonlinearity is added to the short-wave equation [39]. This term breaks integrability while retaining long-wave transport and resonant feedback. The initial field is a direct superposition of two sech pulses. Even at $\gamma = 0$, it is not reflectionless two-soliton scattering data [40]. The centered second-moment, or virial, identity [41] separates dispersive spreading, local quartic overlap, and long-wave feedback. Integrals of these three contributions over the collision interval define a scalar state coordinate. For the adopted two-pulse sech family, this coordinate reproduces the DP or single-peak (SP) morphology with 94.17% agreement.

Direct numerical simulation yields one parameter point at a time. A pointwise survey of the nonintegrable coefficient and relative phase therefore requires many simulations. Machine-learning methods have also been used in studies of integrable systems and nonlinear waves [42−47]. In this Letter, a feed-forward neural network interpolates the three integrals already obtained from 150 numerical results. The interpolation gives a smooth distribution of the state coordinate over the

Received 8 July 2026; accepted 18 September 2026; published 20 October 2026
© 2026 Chinese Physical Society and IOP Publishing Ltd. All rights, including for text and data mining, AI training, and similar technologies, are reserved.

Check for updates

parameter plane. With other parameters fixed, a change in relative phase can move the coordinate across the threshold and change the result between DP and SP forms. Two high-resolution numerical results confirm this phase dependence. The criterion itself follows entirely from the moment identity and does not depend on the network.

To examine collision dynamics away from this ideal integrable setting, we introduce a local cubic envelope perturbation $\gamma|u|^2u$ into the standard two-dimensional LSRI system described above. The cubic term $\gamma|u|^2u$ is analogous to the Kerr-type cubic nonlinearity familiar in nonlinear optics and provides a simple model of additional local nonlinear effects beyond the ideal integrable LSRI reduction. Since physical systems need not satisfy the exact conditions required for integrability, this perturbation provides a controlled setting for studying strong pulse collisions away from the integrable limit. This Letter considers the dimensionless system as

$$\begin{aligned} &\mathrm{i}u_T - u_{XX} + Lu + \gamma|u|^2u = 0, \\ &L_T = L_Y + 2(|u|^2)_X. \end{aligned} \tag{2}$$

At $\gamma = 0$, equation (2) reduces to the standard integrable two-dimensional LSRI system described in Eq. (1). For $\gamma \neq 0$, the cubic term introduces an additional local self-action of the short-wave envelope, which becomes particularly important during strong pulse overlap. Integrable theory mainly characterizes exact coherent structures and their asymptotic ($T \to \infty$) scattering, whereas experiments and numerical simulations directly probe finite-time field configurations. This distinction motivates the finite-time collision-state criterion considered here.

The two spatial directions play different roles in the system. Short-wave dispersion acts along X, whereas the long wave is transported along Y. Let $\rho = |u|^2$; the second equation of Eq. (2) then gives

$$L(X,Y,T) = L(X,Y+T,0) + 2\int_0^T \rho_X(X,Y+T-s,s)\mathrm{d}s. \tag{3}$$

Thus, transported long-wave feedback along Y is coupled into the short-wave evolution. All moments below are integrated over the full (X,Y) domain. They are centered along X because Eq. (2) contains u_{XX} but no u_{YY} term.

On the periodic domain $\mathcal{D} = [0,L_X)\times[0,L_Y)$, the initial fields are

$$\begin{aligned} &u(X,Y,0) = \sum_{j=1}^{2} A_j \,\mathrm{sech}(r_j/w_j)\exp\{\mathrm{i}[k_{x,j}(X-X_j)+\phi_j]\}, \\ &L(X,Y,0) = -2|u(X,Y,0)|^2, \\ &r_j^2 = d_{L_X}(X,X_j)^2 + d_{L_Y}(Y,Y_0)^2, \end{aligned} \tag{4}$$

where d_L denotes the signed shortest periodic displacement. The pulse centers are $X_{1,2} = L_X/2 \mp d_0/2$ and $Y_0 = L_Y/2$. The carrier wavenumbers are $k_{x,1} = -k_x$, $k_{x,2} = k_x$, and $k_{y,1} = k_{y,2} = 0$. The phases are $\phi_1 = 0$ and $\phi_2 = \Delta\phi$, with $\Delta\phi = \phi_2 - \phi_1 \pmod{2\pi}$. The simulations cover $0 \le \Delta\phi \le \pi$; the remaining half-period is not sampled. Equation (4) defines the prescribed radially localized two-sech initial-data family rather than an exact two-soliton solution of the two-dimensional LSRI system. This family is chosen to provide a controlled strong collision dominated by the X direction, consistent with the X-centered moment framework used below. Exact lump initial data are not considered here; for $\gamma \neq 0$, importing an integrable lump profile would additionally mix the collision dynamics with perturbation-induced deformation of the initial coherent structure. Accordingly, the criterion developed below is restricted to this initial-data family and is not assumed to apply to Gaussian profiles, exact lumps, or initial states with relative Y offsets.

A total of 150 direct numerical simulations were performed. Ninety use $\gamma \in \{-1, -0.75, \ldots, 1\}$. They use $k_x \in \{0.6, 0.8, \ldots, 1.4\}$ and $\Delta\phi \in \{0, \pi/2\}$. In this set, $A_1 = 1$, $A_2 = 0.9$, $w_1 = w_2 = 1.2$, and $d_0 = 8$. The other sixty use $-1.1 < \gamma < 1.1$, $0.6 < k_x < 1.4$, and $0 < \Delta\phi < \pi$. They also use $A_1 = 1$, $0.75 < A_2 < 1.05$, $1 < w_1, w_2 < 1.4$, and $7 < d_0 < 9$.

The periodic domain has $L_X = 40$ and $L_Y = 24$. The spatial discretization uses 256×128 Fourier modes, Fourier differentiation, and two-thirds spectral truncation after each nonlinear step [48,49]. Dealiased Strang splitting advances the fields with $\Delta T = 0.005$ up to $T_\mathrm{f} = 7$ [50].

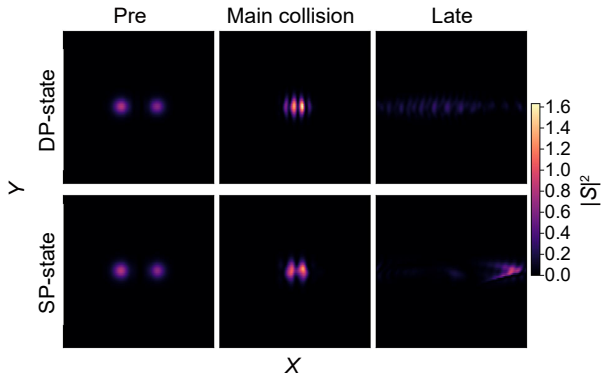

Fig. 1. Representative two-dimensional short-wave intensity $\rho = |u|^2$. The upper and lower rows show DP and SP results. The columns show the field before collision, at maximum overlap, and at late time. Both fields concentrate during overlap. At late time, DP has two separated significant peaks, whereas SP has one dominant peak and weak radiative tails. The common color scale is shown at right.

Two time intervals have distinct purposes. The collision interval contains the strongest pulse overlap and supplies the integrals in the moment criterion. The late observation interval begins after the main interaction and identifies only the finite-time intensity morphology. Define $T_\mathrm{c}^{(0)} = d_0/(4k_x)$ and $\tau_w = (w_1+w_2)/(8k_x)$. The collision time T_c maximizes $Q(T) = \iint_{\mathcal{D}} \rho^2 \mathrm{d}X\mathrm{d}Y$ subject to

$$|T - T_\mathrm{c}^{(0)}| \le \max(1, 4\tau_w). \tag{5}$$

The collision interval is $[T_-, T_+] = [T_\mathrm{c} - 2\tau_w, T_\mathrm{c} + 2\tau_w]$. It is truncated only at the endpoints of the total simulation. The quantity $Q(T)$ measures short-wave overlap. It increases as the two localized intensity cores approach and reaches a principal maximum near their closest encounter. The restricted search prevents selection of a later maximum caused by radiation.

For $d_0 = 8$, $k_x = 1.2$, and $w_1 = w_2 = 1.2$, one has $T_\mathrm{c}^{(0)} = 5/3$ and $\tau_w = 1/4$. The search interval is then $2/3 \le T \le 8/3$, and the integration interval is $[T_\mathrm{c} - 0.5, T_\mathrm{c} + 0.5]$. The late interval is $[T_\mathrm{l}, T_\mathrm{f}]$, where $T_\mathrm{l} = \max(T_\mathrm{c} + 4\tau_w, 0.68T_\mathrm{f})$. Its delayed start reduces the influence of the main overlap on the morphology definition.

At each recorded late time, ρ is smoothed by a periodic Gaussian filter with a standard deviation of 0.8 grid points. Connected components are then extracted from $\rho \ge 0.28\rho_{\max}$. A component is significant when it contains at least 3.5% of the total smoothed intensity mass. Two-component morphology also requires a secondary-to-primary mass ratio of at least 0.12 and a combined mass fraction of at least 0.35.

Let P_2^{late} be the fraction of late times with two significant components. Let D_2^{late} be their median centroid separation divided by $w_{\mathrm{eff}} = (w_1+w_2)/2$. A result is identified as DP when $P_2^{\mathrm{late}} \ge 0.75$ and $D_2^{\mathrm{late}} \ge 2$. It is SP when $P_2^{\mathrm{late}} \le 0.25$ and $D_2^{\mathrm{late}} \le 1.2$. Results meeting neither definition are retained but do not determine the threshold.

The left and middle columns of Fig. 1 show the initial state and transient overlap. The middle time follows the maximum-overlap rule rather than visual selection. In the right column, DP has two separated high-intensity cores, whereas SP has one. The surrounding low-intensity structures are radiation. The main intensity remains near $Y = L_Y/2$, while radiation and long-wave-mediated deformation extend in both directions. The evolution is therefore two-dimensional although the second moment is centered along X.

Equation (2) gives the continuity relation

$$\rho_T = 2\partial_X \mathrm{Im}(u^* u_X). \tag{6}$$

Integration over the periodic domain $\mathcal{D}$ cancels the X-boundary term.

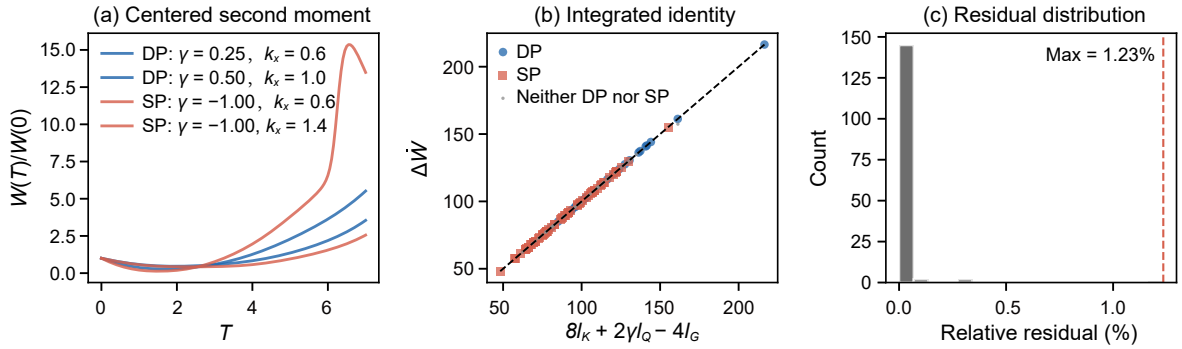

Fig. 2. Checks of the moment identity using direct numerical simulations. (a) Representative normalized second moments for DP and SP results. Their continued growth shows that $W(T)$ alone does not identify late morphology. (b) The two sides of Eq. (10) for all 150 results. (c) Relative integrated residual, with a maximum of 1.23%. The maximum relative mass drift is 1.20×10^{-3}, and the maximum high-frequency spectral-tail fraction is 0.117.

Hence, the mass $M=\iint_{\mathcal{D}}\rho\mathrm{d}X\mathrm{d}Y$ is conserved. Define

$$\bar{X}=\frac{1}{M}\iint_{\mathcal{D}}X\rho\mathrm{d}X\mathrm{d}Y,\quad W=\iint_{\mathcal{D}}(X-\bar{X})^2\rho\mathrm{d}X\mathrm{d}Y. \tag{7}$$

Here W is the centered second-order spatial moment of the short-wave intensity $\rho=|u|^2$ along the X direction. It measures the spatial spreading of the short-wave packet about its intensity centroid $\bar{X}$. Since M is conserved, a larger W corresponds to a more spatially spread short-wave distribution, whereas a smaller W indicates a more concentrated distribution. Periodic displacement from the domain center is used in the numerical evaluation. The quantities in the moment balance are

$$\begin{aligned}P&=\iint_{\mathcal{D}}\mathrm{Im}(u^*u_X)\mathrm{d}X\mathrm{d}Y,\\ K&=\iint_{\mathcal{D}}|u_X|^2\mathrm{d}X\mathrm{d}Y-\frac{P^2}{M},\\ Q&=\iint_{\mathcal{D}}|u|^4\mathrm{d}X\mathrm{d}Y,\\ G&=\iint_{\mathcal{D}}(X-\bar{X})|u|^2L_X\mathrm{d}X\mathrm{d}Y.\end{aligned} \tag{8}$$

Here K is the short-wave gradient contribution after removal of center-of-mass motion. The quantity Q measures local quartic overlap. The quantity G measures coupling to the X gradient of the long-wave field. Differentiation of Eq. (7) and integration by parts give the virial identity

$$\ddot{W}=8K+2\gamma Q-4G. \tag{9}$$

Physically, $\dot{W}$ is the spreading rate of the short-wave intensity distribution along X, and $\ddot{W}$ is its spreading acceleration. Equation (9) therefore shows that this acceleration is determined by three competing effects: dispersive spreading through $8K$, the local quartic-overlap contribution of the cubic perturbation through $2\gamma Q$, and long-wave feedback through $-4G$. All terms in Eq. (9) are two-dimensional integrals. Further integration over $[T_-,T_+]$ gives

$$\begin{aligned}\Delta\dot{W}&=8I_K+2\gamma I_Q-4I_G,\\ I_K&=\int_{T_-}^{T_+}K(T)\mathrm{d}T,\\ I_Q&=\int_{T_-}^{T_+}Q(T)\mathrm{d}T,\\ I_G&=\int_{T_-}^{T_+}G(T)\mathrm{d}T.\end{aligned} \tag{10}$$

Figure 2(a) shows that the instantaneous second moment $W(T)$ alone cannot distinguish the late-time DP and SP morphologies: the two outcomes can exhibit comparable spatial spreading. The relevant information is instead the total change in spreading rate, $\Delta\dot{W}$, accumulated over the main collision window. Equation (10) decomposes this change into the integrated contributions of dispersive spreading, local quartic overlap, and long-wave feedback. Figures 2(b) and 2(c) verify this integrated balance over the full set, and the small residual supports the numerical evaluation of the three contributions.

Dividing the nondispersive part of Eq. (10) by $-8I_K$ gives $-\gamma I_Q/(4I_K)+I_G/(2I_K)$. This dimensionless combination compares the local cubic contribution and long-wave feedback with centered short-wave spreading. The leading even harmonic represents the measured relative-phase dependence. The 103 numerical results that meet either morphology definition give

$$C_{\mathrm{SC}}=-\frac{\gamma I_Q}{4I_K}+\frac{I_G}{2I_K}-0.061\cos\Delta\phi,\quad C_*=-0.183529. \tag{11}$$

For the profiles, ranges, and time intervals stated above, $C_{\mathrm{SC}}<C_*$ corresponds to DP and $C_{\mathrm{SC}}\geq C_*$ corresponds to SP. The threshold is empirical and belongs to this finite initial-data family. It is not an asymptotic boundary for arbitrary LSRI data.

Figure 3(a) shows the parameter ranges. Figure 3(b) places the state coordinate beside the late two-component fraction. Figure 3(c) separates the three terms in the criterion. Figure 3(d) gives the direct comparison.

Balanced agreement is the mean of the correct fractions in the DP and SP groups. The $\gamma=0$ subset contains ten results from the same two-pulse initial-data family. Five meet the SP definition, and five meet neither definition. None meets the strict DP definition for $T\leq7$. The criterion also identifies the former five as SP.

Equation (4) remains a prescribed sech superposition rather than exact reflectionless two-soliton scattering data as $\gamma\to0$. The occurrence of an SP morphology at $\gamma=0$ therefore does not conflict with the elastic scattering of exact integrable solitons. Setting $\gamma=0$ restores the integrable LSRI equation, but the prescribed initial state can generate radiation and transient reshaping, allowing a SP morphology to occur within the finite observation interval. The $\gamma=0$ results thus test the present initial-data family rather than exact two-soliton collisions.

Twelve representative results were recomputed with 320×160 modes and a smaller time step. Six were also recomputed with a fourth-order Runge–Kutta–Fourier scheme. Their morphology and criterion results were unchanged. These tests address discretization only within the stated parameter ranges.

A feed-forward neural network interpolates between six parameters $\boldsymbol{\mu}=(\gamma,k_x,\Delta\phi,A_2/A_1,w_2/w_1,d_0)$ and the computed integrals I_K, I_Q, and I_G. All 150 direct results enter the interpolation, and no independent test set is used. The smooth background in Fig. 4 therefore displays parameter dependence only. It is not additional numerical evidence. The interpolation does not determine the coefficient 0.061, the threshold C_*, any morphology, or the 97/103 agreement.

For the relative-phase comparison, $k_x=1.2$, $A_2/A_1=0.9$, $w_2/w_1=1$,

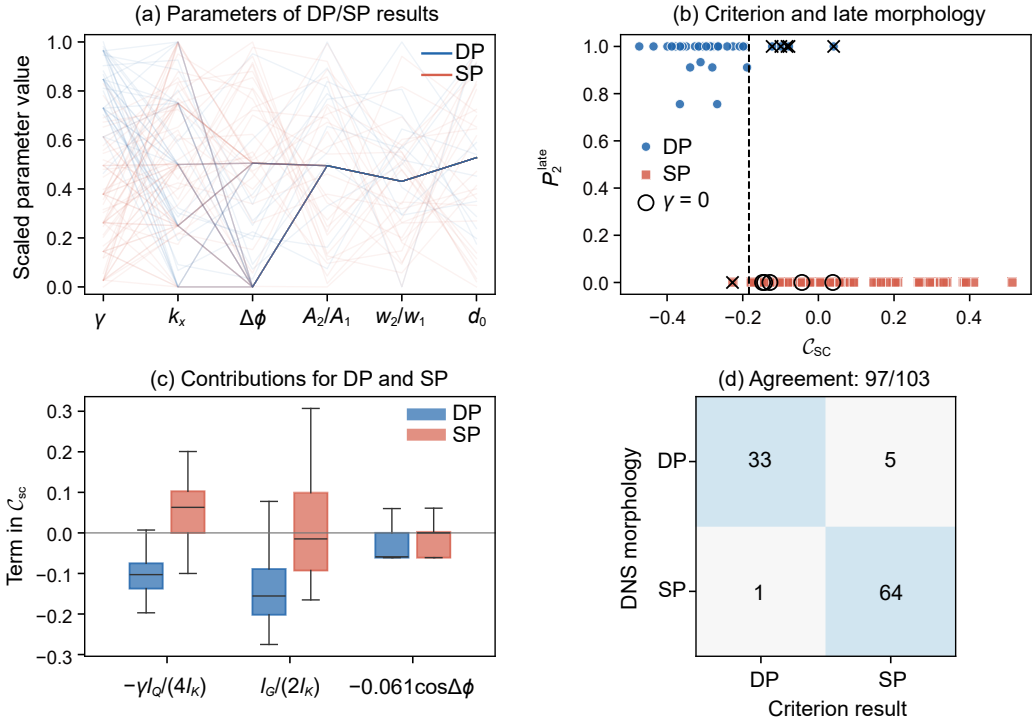

Fig. 3. Comparison of the moment criterion with the 103 direct numerical results that meet a DP or SP definition. (a) Ranges of the six varying profile parameters. (b) State coordinate and late two-component fraction. The dashed line is the threshold. Open circles mark the five $\gamma = 0$ SP results, and crosses mark disagreements. (c) Three contributions to Eq. (11). (d) Direct morphology and criterion result. The diagonal contains 97 results, giving 94.17% overall and 92.65% balanced agreement.

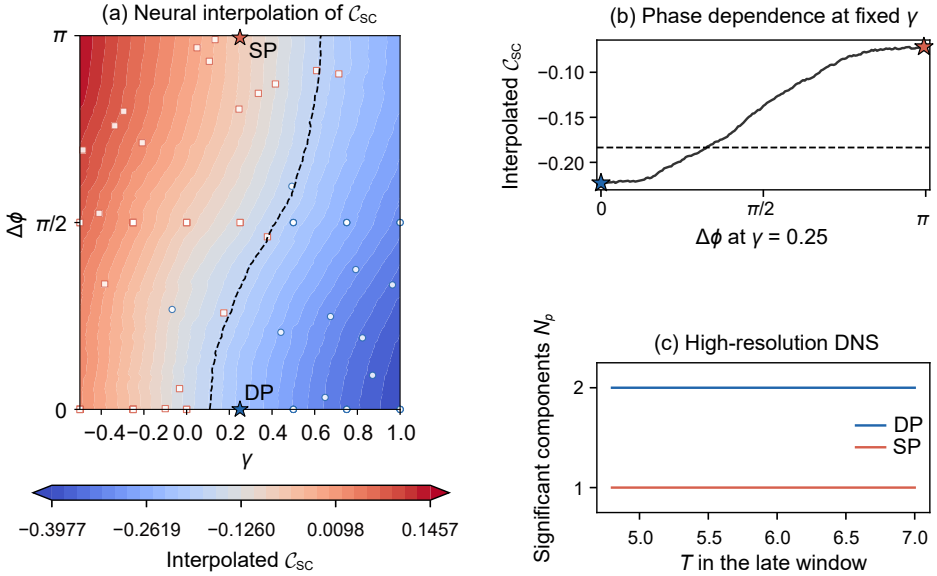

Fig. 4. Relative-phase dependence for fixed $k_x = 1.2$, $A_2/A_1 = 0.9$, $w_2/w_1 = 1$, and $d_0 = 8$. (a) Interpolated state coordinate. The dashed curve is the threshold. Open circles and squares are direct DP and SP results, and stars mark two high-resolution results at $\gamma = 0.25$. (b) State coordinate at $\gamma = 0.25$. (c) Number of significant components during the late interval for 320×160 modes and $\Delta T = 0.0025$. At $\Delta\phi = 0$, the two-component fraction, normalized separation, and state coordinate are 0.9111, 6.8861, and −0.2804. At $\Delta\phi = 3.124139 \simeq 0.994\pi$, they are 0, 0, and −0.0104.

and $d_0 = 8$ are fixed. Only γ and $\Delta\phi$ vary. Substitution of the interpolated integrals into Eq. (11) gives the background over $-0.5 \le \gamma \le 1$ and $0 \le \Delta\phi \le \pi$. Every overlaid circle, square, and star is a direct numerical result.

The two selected phase points lie on opposite sides of C_* and show DP and SP morphologies. Their relative mass drifts are 1.60×10^{-3} and 1.58×10^{-3}. Their integrated moment residuals are 2.40×10^{-5} and 1.43×10^{-4}. These results establish phase dependence only for the fixed parameters above. They do not establish a criterion based on phase alone.

In summary, the centered second-moment identity separates short-wave dispersion, local quartic overlap, and transported long-wave feedback in a two-dimensional LSRI collision. Collision-interval integrals of these terms give a scalar criterion for the adopted two-pulse initial-data family. The criterion agrees with 97 of the 103 results that meet a DP or SP definition. The 94.17% agreement is evaluated on the same data that determine the threshold. It therefore describes finite-time morphology but is not an independent validation result.

The identity also explains each term in the criterion. The integral I_K represents centered short-wave spreading. The term γI_Q represents

the accumulated local cubic contribution during pulse overlap. The integral I_G represents accumulated long-wave feedback. Their relative magnitudes describe how the collision changes the spreading rate. The phase contribution is usually smaller. Near the threshold, however, it can still change the final morphology. Results outside both strict definitions require inspection of the full field evolution.

The integrable limit depends on the initial data. Setting $\gamma = 0$ restores the integrable equation but does not create reflectionless two-soliton scattering data. Such a comparison requires the corresponding exact LSRI scattering data as the initial condition. The conclusions of this Letter are restricted to the prescribed radially localized two-sech initial-data family with a common Y center and zero transverse carrier wavenumber. They are not assumed to extend to Gaussian profiles, exact lumps, or initial states with relative Y offsets. They also apply only to the stated parameter ranges and $T \leq 7$. Thus, DP and SP denote finite-time morphologies, not $T \to \infty$ asymptotic states. Longer times, transverse offsets, other initial profiles, and links to spectral asymptotic regions remain open. The neural interpolation only displays phase dependence. The principal evidence is supplied by direct simulations, the virial identity, the discretization tests, and the two high-resolution results.

Acknowledgements

This work was supported by the Fundamental Research Funds for the Beijing University of Posts and Telecommunications (Grant No. 2025JCTP01), the National Key Research and Development Program of China (Grant No. 2022YFB4601101), and the National Natural Science Foundation of China (Grant No. 12261131495).

References

[1] Yan Y Y and Liu W J 2021 *Chin. Phys. Lett.* **38** 094201
[2] Qiu W X, Si Z Z, Mou D S, Dai C Q, Li J T, and Liu W 2025 *Nonlinear Dyn.* **113** 4063
[3] Yuan C L, Liu W J, Yang H J, and Tian Y 2025 *Nonlinear Dyn.* **113** 15273
[4] Kumar G A, Kanna T, and Vijayajayanthi M 2025 *Physica D* **481** 134811
[5] Stalin S and Lakshmanan M 2025 *Chaos Solitons Fractals* **200** 117132
[6] Benney D J 1976 *Stud. Appl. Math.* **55** 93
[7] Benney D J 1977 *Stud. Appl. Math.* **56** 81
[8] Yajima N and Oikawa M 1976 *Prog. Theor. Phys.* **56** 1719
[9] Djordjevic V D and Redekopp L G 1977 *J. Fluid Mech.* **79** 703
[10] Ohta Y, Maruno K I, and Oikawa M 2007 *J. Phys. A: Math. Theor.* **40** 7659
[11] Rao J, Porsezian K, He J, and Kanna T 2018 *Proc. R. Soc. A* **474** 20170627
[12] Rao J, Kanna T, Mihalache D, and He J 2022 *Physica D* **439** 133281
[13] Kanna T, Vijayajayanthi M, Sakkaravarthi K, and Lakshmanan M 2009 *J. Phys. A: Math. Theor.* **42** 115103
[14] Kanna T, Sakkaravarthi K, and Tamilselvan K 2013 *Phys. Rev. E* **88** 062921
[15] Chen J C, Feng B F, Chen Y, and Ma Z Y 2017 *Nonlinear Dyn.* **88** 1273
[16] Rao J, Kanna T, and He J 2025 *Chaos Solitons Fractals* **200** 117133
[17] Caso-Huerta M, Feng B F, Lombardo S, Maruno K I, and Sommacal M 2025 *Wave Motion* **134** 103511
[18] Li W, Zhang Y, and Yang X 2024 *Phys. Scr.* **99** 075246
[19] Zhu X J and Zhu X M 2026 *J. Phys. A: Math. Theor.* **59** 185701
[20] Yang J 2026 *Eur. Phys. J. Plus* **141** 322
[21] Rao J, Kanna T, and He J 2022 *Proc. R. Soc. A* **478** 20210777
[22] Pu J C and Chen Y 2024 *Physica D* **467** 134262
[23] Chen J C, Zhang X F, Li B, and Chen Y 2012 *Chin. Phys. Lett.* **29** 070303
[24] Chen J C, Chen Y, Feng B F, and Zhu H M 2014 *Chin. Phys. Lett.* **31** 110502
[25] Hu X R, Chen J C, and Chen Y 2015 *Chin. Phys. Lett.* **32** 070201
[26] Zhao B, Dai C Q, and Zhang J F 2012 *Chin. Phys. Lett.* **29** 084201
[27] Cao Q H and Dai C Q 2021 *Chin. Phys. Lett.* **38** 090501
[28] Liu J H, Geng K L, and Dai C Q 2025 *Chin. Phys. Lett.* **42** 040201
[29] Chen J C, Chen Y, Feng B F, and Maruno K I 2015 *Phys. Lett. A* **379** 1510
[30] Sun W R, Malomed B A, and Li J H 2024 *Phys. Rev. E* **109** 024209
[31] Li J B, Yang Y, Liu C, and Akhmediev N 2026 *Phys. Rev. E* **113** 054210
[32] Liu P, Chen Y, and Chai X D 2025 *Chaos* **35** 013120
[33] Liu L, Sun W R, and Malomed B A 2023 *Phys. Rev. Lett.* **131** 093801
[34] Liu L, Sun W R, Malomed B A, and Kevrekidis P G 2023 *Phys. Rev. A* **108** 033504
[35] Xue L P and Zhang Q F 2024 *Physica D* **470** 134372
[36] Huang L, Wang D S, and Zhu X 2026 *Math. Ann.* **395** 18
[37] Wang D S and Zhu X 2026 *SIAM J. Math. Anal.* **58** 3325
[38] Wang D S and Yan P 2025 *Nonlinearity* **38** 125006
[39] Hasegawa A and Tappert F 1973 *Appl. Phys. Lett.* **23** 142
[40] Satsuma J and Yajima N 1974 *Prog. Theor. Phys. Suppl.* **55** 284
[41] Glassey R T 1977 *J. Math. Phys.* **18** 1794
[42] Pu J C and Chen Y 2023 *Commun. Nonlinear Sci. Numer. Simul.* **118** 107051
[43] Peng W Q and Chen Y 2024 *Chaos* **34** 043124
[44] Zhou H and Chen Y 2026 *Chin. Phys. Lett.* **43** 040003
[45] Liu X M, Zhang Z Y, and Liu W J 2023 *Chin. Phys. Lett.* **40** 070501
[46] Zhou H, Zhang Z Y, Liu M W, Qi F H, and Liu W J 2025 *Chin. Phys. Lett.* **42** 070001
[47] Thulasidharan K, Vishnu Priya N, Monisha S, and Senthilvelan M 2024 *Phys. Lett. A* **511** 129551
[48] Taha T R and Ablowitz M I 1984 *J. Comput. Phys.* **55** 203
[49] Weideman J A C and Herbst B M 1986 *SIAM J. Numer. Anal.* **23** 485
[50] Strang G 1968 *SIAM J. Numer. Anal.* **5** 506